

Article

The REE-Induced Absorption and Luminescence in Yellow Gem-Quality Durango-Type Hydroxylapatite from Muránska Dlhá Lúka, Slovakia

Peter Bačík ^{1,*} , Jana Fridrichová ¹, Ján Štubňa ², Tomáš Bancík ³, Ľudmila Illášová ², Helena Pálková ⁴, Radek Škoda ⁵ , Tomáš Mikuš ⁶, Stanislava Milovská ⁶, Tomáš Vaculovič ⁷ and Peter Sečkář ¹

¹ Department of Mineralogy and Petrology, Faculty of Natural Sciences, Comenius University in Bratislava, Ilkovičova 6, Mlynská dolina, Bratislava 84215, Slovakia; jana.fridrichova@uniba.sk (J.F.); seckar1@gmail.com (P.S.)

² Gemmological Laboratory, Department of Geography and Regional Development, Faculty of Natural Sciences, Constantine the Philosopher University in Nitra, Nábrežie mládeže 91, Nitra 94974, Slovakia; jstubna@ukf.sk (J.Š.); lillasova@ukf.sk (L.L.)

³ Slovak Mineralogical Society, Viestova 26, Banská Bystrica 97401, Slovakia; tomas.bancik@gmail.com

⁴ Institute of Inorganic Chemistry Slovak Academy of Sciences, Dúbravská cesta 9, Bratislava 84536, Slovakia; uachpalk@savba.sk

⁵ Department of Geological Sciences, Masaryk University, Kotlářská 2, 61137 Brno, Czech Republic; rskoda@sci.muni.cz

⁶ Earth Science Institute of the Slovak Academy of Sciences, Ďumbierska 1, Banská Bystrica 97401, Slovakia; mikus@savbb.sk (T.M.); milovska@savbb.sk (S.M.)

⁷ Central European Institute of Technology, Masaryk University, Kamenice 5, 62500 Brno, Czech Republic; tomas.vaculovic@ceitec.muni.cz

* Correspondence: peter.bacik@uniba.sk

Received: 16 October 2020; Accepted: 8 November 2020; Published: 11 November 2020



Abstract: In talc-magnesite veins in serpentinite near Muránska Dlhá Lúka (MDL), Slovakia, yellow euhedral to subhedral crystals apatite of a gem quality occur. It has a composition of hydroxylapatite with F^- varying between 0.29 and 0.34 apfu, Cl^- in range of 0.02–0.05 apfu and calculated OH^- content between 0.62–0.68 apfu. Moreover, $[CO_3]^{2-}$ molecules were identified by FTIR and Raman spectroscopy. MDL apatite contains only up to 0.003 apfu As^{5+} and Si^{4+} substituting for P^{5+} ; Ca is substituted by small amount of Na, Fe^{2+} , Mn^{2+} (all up to 0.006 apfu), and Rare Earth Elements (REE—in total up to 0.017 apfu). Compared to trace-element composition of similar apatites from Durango, Mexico, the REE content in MDL apatite is around ten times lower with $Nd > Ce \gg La$, its chondrite-normalized REE pattern has almost a horizontal slope and larger negative Eu anomaly. The MDL apatite is richer in Mn, Pb and Li, but poorer in As, V, Th and U. The concentrations of Sr and Y are similar. In the optical absorption spectra, the most prominent bands are at 585–590 nm (Nd^{3+}) and between 600 and 800 nm (Mn^{2+} , Ce^{3+} - SiO_3^{3-} photochromic center and Nd^{3+}). The photoluminescence spectrum of MDL apatite shows bands between 550 and 620 nm (Dy^{3+} , Sm^{3+} , Pr^{3+} and also Mn^{2+}) which likely enhance its yellow color. MDL hydroxylapatite likely formed from fluids derived from granitic rocks as evidenced by the chondrite-normalized REE patterns, Li, Mn and Y concentrations. The Sr content reflects the host-rock serpentinite composition. Fluids for its crystallization were likely derived from Muráň complex orthogneisses by the Alpine deformation and recrystallization in greenschist to lower amphibolite facies.

Keywords: hydroxylapatite; REE; Raman spectroscopy; photoluminescence; optical absorption spectroscopy; gem

1. Introduction

The apatite-supergroup minerals are the most abundant P-bearing minerals, the tenth most abundant mineral group in the Earth's crust and commonly occur in all geological environments [1,2]. The apatite supergroup contains minerals with the structural formula ${}^{\text{IX}}\text{M}_1\text{M}_2\text{M}_3(\text{IV}\text{TO}_4)_3\text{X}$ [1]. Two structurally different M sites, ninefold coordinated M_1O_9 and sevenfold coordinated $\text{M}_2\text{O}_6\text{X}$ polyhedrons are dominantly occupied by Ca [3,4]. Calcium can be substituted by large cations including Pb, Ba, Sr, Na, and also Rare Earth Elements (REE) [1]. The anionic X site is mainly occupied by OH, F, and Cl. The tetrahedral T site is largely dominated by P with possible substitutions by As, V, S and Si which results in division of the supergroup into five groups—apatite, hedyphane, belovite (all include phosphates, vanadates and arsenates), britholite (silicate) and ellestadite (silicate, sulphate) groups [1].

Gem apatites have very variable colors including violet, blue, green, yellow-orange and brown. The most abundant colors are blue and green, however, despite numerous investigations, the origin of these colors is ambiguous [5,6]. The blue natural apatite is the most popular among others in a gemstone market due to their similar appearance to blue tourmaline type of “Paraiba” [7]. Gem-quality apatite can be found, e.g., in Mozambique [8], Kenya [9], Brazil [10], Bolivia [11], Canada [12], Iran [13], Namibia [14], Mexico [15]. Some of them also have a cat's eye effect [16–19]. Remarkable apatites from Kazakhstan display a color change [20].

Apatite from Muránska Dlhá Lúka forms almost golden yellow, usually euhedral, gem-quality crystals similar to the famous Durango apatites. Durango apatite is known to mineral collectors for its yellow color, transparency, and perfect crystal form. Durango fluorapatite crystals are found in the martite of the ore body in several modes of occurrences (fissures or cavities in the martite, less commonly embedded in martite, locally in veinlets) in the Cerro de Mercado (Iron Mountains) near the city of Durango, the largest deposit of iron ore in Mexico [21].

This study brings detailed mineralogical, crystal-chemical and spectroscopic characterization of yellow gem-quality apatite from Muránska Dlhá Lúka (MDL) by using a variety of analytical methods for determination of chemical composition, spectroscopic properties, color and photoluminescence. Moreover, detailed investigation allows us to describe MDL apatite as a gemstone with a distinguished origin based on trace-element composition and spectroscopic properties. In conclusion, based on the collected data, it is possible to propose genetic conditions of MDL apatite.

2. Geological Setting

The Variscan basement of the Western Carpathians is exposed in Cretaceous Tatric, Veporic and Gemeric basement-cover units [22–24]. Pre-Alpine tectonometamorphic evolution was related to the subduction-collision processes during Variscan orogeny, resulting from convergence, accretion and amalgamation of crustal blocks derived from Gondwana with Laurussia [24,25]. The Tatric and Veporic crystalline basement is defined by the Variscan Upper Unit (Tatra Nappe) thrust over the Variscan Middle Unit (Hron Nappe) [23,26]. The Upper Unit contains paragneisses, granitic orthogneisses, amphibolites, rare calc-silicate marbles, migmatites and meso-Variscan granitic plutons. The Middle Unit is composed of micaschists to gneisses. The base of the Upper Unit contains layered amphibolites and kyanite-garnet gneisses with lenses of metagabbros, eclogites and metaperidotites as a typical lower-crustal complex [27,28]. The orthogneisses of the Variscan Upper Unit contain isolated bodies of serpentinite with talc. The formation of talc zone and associated minerals is younger in time than serpentinitization processes. It is associated with the action of CO_2 -enriched hydrothermal solutions during regional metamorphism of the complex [29].

Apatite from Muránska Dlhá Lúka occurs in talc-magnesite veins in the serpentinite body which can relate to the fluid regime during regional metamorphic events. Early Variscan (eo-Variscan) subduction/collision event is dated from 430 to 390 Ma in the layered amphibolites and associated orthogneisses by the U/Pb zircon ages, later post-collision extension partial melting of the layered amphibolites and orthogneisses occurred between 370 and 350 Ma [30,31]. P-T conditions of 16–20 kbar and 645–725 °C were estimated from an eclogitic lens in the migmatitic orthogneiss. The host orthogneiss

reflects 11–4 kbar, 740–532 °C exhumation conditions, and the garnet-kyanite-phengite-rutile mineral assemblage may well represent peak burial stage [32]. The Alpine deformation and recrystallization occurred in medium pressure (MP) greenschist to lower amphibolite facies (T_{\max} 500–530 °C, P_{\max} 8–9 kbar [27]). The Alpine tectono-metamorphic overprint is related to Cretaceous collision wedge evolution limited by subduction suture zones after closure of the Tethyan Meliatic and Penninic Oceans and dated between 130 and 50 Ma by the ^{40}Ar - ^{39}Ar white mica ages [33].

Muránska Dlhá Lúka lies in the northern part of the Stolické Hills 5 km northwest of the county town Revúca at an altitude of 345 m above sea level. The area is built by biotitic granodiorites to granites, biotitic to bi-mica schists with bodies of amphibolites and serpentinites of the Kohút zone of the Veporic Superunit crystalline basement [29] (Figure 1). A talc and serpentinite (used as a building stone) deposit is located ca. 2 km west of the village and approximately 600 m east of the Kamenná hill (718 m above sea level) at an altitude of 550–580 m above sea level. It was opened by a quarry and two galleries between the years 1920–1955. The deposit was explored and mined in 1953 and 1954 [34].

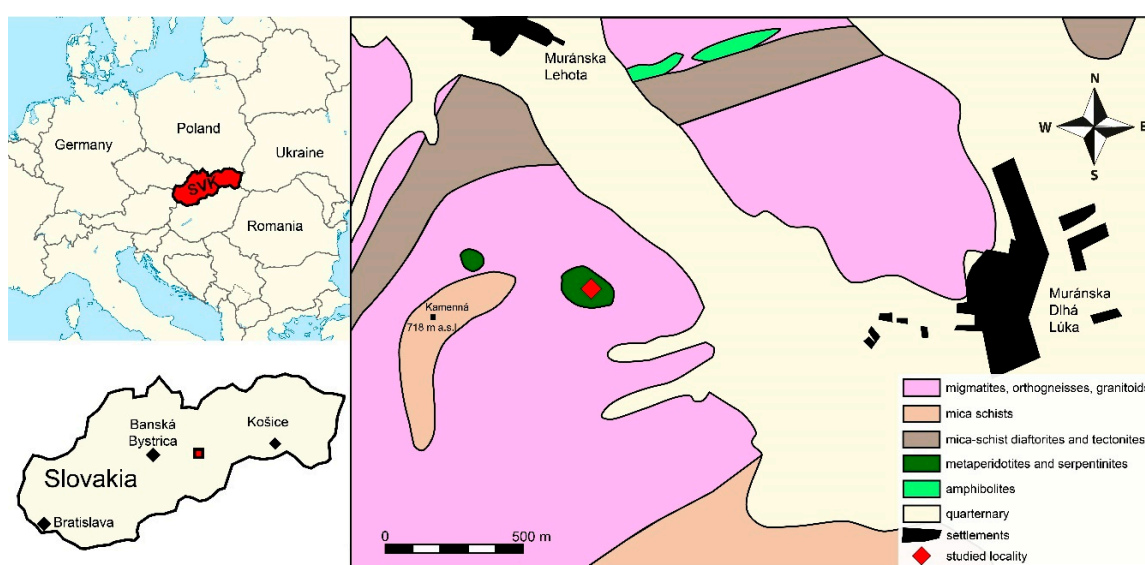


Figure 1. Geological sketch map of the Muránska Dlhá Lúka area (modified after [35]).

The serpentinite deposit is 140 m long with a maximum thickness of 35 m. The inclination depth is 80 m. Reaction metasomatic contacts containing talc, which were the subject of mining, are developed at the edges of the deposit (Figure 2). This zone varies from 1.7 to about 6 m in the deep wedging of the serpentinite body. Talc reserves have been estimated to several tens of thousands tons. Talc materials have a high Fe_2O_3 content and, therefore, have had virtually no industrial significance in the past [34].

Apatite is one of the minerals occurring in white to green talc veins. Apatite was found in the talc vein in the central part of the quarry. The vein of talc with apatite is 5 to 30 cm thick. Apatite is the part of the hydrothermal paragenesis and is associated with dolomite (forming rhombohedral crystals up to 5 cm in size), clinocllore and rare magnetite. The color of apatite varies from olive green to a yellow-gold, reminiscent of a heliodor (Figure 3). Smaller crystals are transparent, larger crystals are usually translucent [36].



Figure 2. Vein of green talc in the serpentinite body at Muránska Dlhá Lúka deposit (Photo by T. Bancík).



Figure 3. Yellow crystals of apatite: (a) hexagonal prismatic crystal in green talc; (b) hexagonal prismatic crystal in white to grey magnesite; (c) aggregate of apatite crystals in green talc. Photo by T. Bancík.

3. Materials and Methods

Studied samples of MDL apatite include one crystal cut and put into the polished section and the remaining part of the crystal fragment for electron-microprobe analysis (EMPA) and laser-ablation inductively coupled plasma mass spectrometry (LA-ICP-MS), the remaining part of the crystal fragment was powdered for Fourier transform infrared (FTIR) spectroscopy. Five other apatite crystals (Figure 4) were cut as gemstones and measured with optical absorption spectroscopy (OAS).

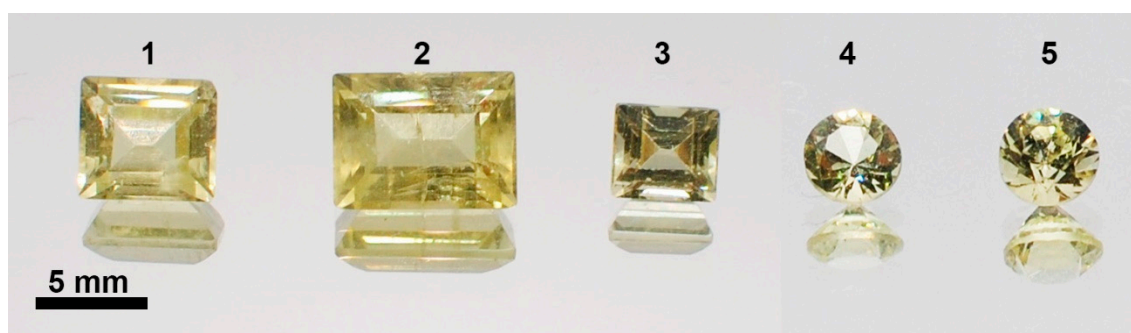


Figure 4. Apatite from Muránska Dlhá Lúka cut as gemstones—samples 1–5 according to Table 1. Photo by J. Štubňa.

Chemical composition of apatite on the crystal fragment was measured using a JEOL JXA—8530F equipment at the Institute of the Earth Sciences of the Slovak Academy of Sciences in Banská Bystrica (Slovakia). The following conditions were used: accelerating voltage 15 kV, probe current 20 nA and beam diameter 5 μm and ZAF (Z—atomic number, A—absorption, F—fluorescence) matrix correction was used. The EPMA was calibrated by the natural and synthetic standards. Used standards, X-ray lines, and detection limits (in ppm) were: Ca ($K\alpha$, 57)—apatite, U ($M\beta$, 208)— UO_2 , S ($K\alpha$, 79)—barite, Th ($M\alpha$, 138)—thorianite, Pb ($M\beta$, 257)—crocoite, Cl ($K\alpha$, 52)—tugtupite, Zr ($L\beta$, 201)—cubic zirconia, P ($K\alpha$, 176)—apatite, Y ($L\alpha$, 218)— YPO_4 , F ($K\alpha$, 274)—fluorite, Sr ($L\alpha$, 427)—celestite, Si ($K\alpha$, 158)—diopside, Al ($K\alpha$, 115)—albite, As ($L\alpha$, 342)—GaAs, Na ($K\alpha$, 143)—albite, Lu ($L\alpha$, 358)— LuPO_4 , Tm ($L\beta$, 622)— TmPO_4 , Ho ($L\beta$, 622)— HoPO_4 , Yb ($L\alpha$, 329)— YbPO_4 , Er ($L\alpha$, 303)— ErPO_4 , Gd ($L\beta$, 506)— GdPO_4 , Dy ($L\alpha$, 595)— DyPO_4 , Tb ($L\alpha$, 260)— TbPO_4 , Sm ($L\beta$, 460)— SmPO_4 , Eu ($L\alpha$, 252)— EuPO_4 , Pr ($L\beta$, 422)— PrPO_4 , Nd ($L\alpha$, 231)— NdPO_4 , Ce ($L\alpha$, 234)— CePO_4 , La ($L\alpha$, 254)— LaPO_4 , Ti ($K\alpha$, 504)—rutile, Mn ($K\alpha$, 341)—rhodonite, Sc ($K\alpha$, 1720)— ScVO_4 , V ($K\alpha$, 359)— ScVO_4 , Ba ($L\alpha$, 1201)—barite. The apatite chemical formula was calculated based on eight cations.

Instrumentation for LA-ICP-MS at the Department of Chemistry, Masaryk University, Brno, Czech Republic consists of a UP 213 laser ablation system (New Wave Research, Inc., Fremont, CA, USA) and Agilent 7500 CE ICP-MS spectrometer (Agilent Technologies, Santa Clara, CA, USA). A commercial Q-switched Nd-YAG laser-ablation device works at the fifth harmonic frequency corresponding to 213 nm wavelength. The ablation device is equipped with a programmable XYZ-stage to move the sample along a programmed trajectory during ablation. Target visual inspection and photographic documentation were achieved by built-in microscope/CCD-camera system. A sample was enclosed in the SuperCell (New Wave Res., Fremont, CA, USA) and was ablated by the laser beam, which was focused onto the sample surface through a quartz window. The ablation cell was flushed with helium carrier gas which transported the laser-induced aerosol to the inductively coupled plasma (1 L min^{-1}). Sample argon gas flow was admixed with the helium carrier gas flow after laser ablation cell to 1.6 L min^{-1} total gas flow. NIST SRM 610 silicate glass reference material was used to optimize the gas flow rates, the sampling depth and MS electrostatic lens voltage in LA-ICP-MS conditions. This provided maximum signal to noise ratio and minimum oxide formation (ThO^+/Th^+ count ratio 0.2%, U^+/Th^+ counts ratio 1.1%). Laser ablation required $100 \mu\text{m}$ laser spot diameter, 8 J cm^{-2} laser fluence and 20 Hz repetition rate. The fixed sample position during laser ablation enabled 60 s hole-drilling duration for each spot. All element measurements were normalized on the sum of oxides.

FTIR spectra in the middle IR region ($4000\text{--}400 \text{ cm}^{-1}$) were obtained from powdered sample using a Fourier-transform infrared Nicolet 6700 spectrometer (Thermo Electron Scientific Instruments LLC, Madison, WI, USA) equipped with a DTGS (deuterated triglycine sulphate) detector and a KBr beam splitter. Spectra were collected by coaddition of 128 scans at a resolution of 4 cm^{-1} . The KBr pressed-disc technique (1 mg of sample and 200 mg of KBr) was employed. The discs were heated

in a furnace overnight at 150 °C and spectra were measured using a spectrometer purged with dry air to minimize the water adsorbed on both the sample and KBr. The OMNICTM Thermo Electron Corporation software package (Version 8.3, Thermo Fisher Scientific Inc., Waltham, MA, USA) was used for spectra handling and baseline subtraction.

Raman analyses were performed on the LabRAM-HR Evolution (Horiba Jobin-Yvon, Longjumeau, France) spectrometer system with a Peltier cooled CCD (charge-coupled device) detector and Olympus BX-41 microscope (Department of Geological Sciences, Masaryk University, Brno, Czech Republic). Raman spectra were excited by blue diode laser (473 nm) with power of 2.5 mW in the range of 50–4000 cm^{-1} were collected from each stone using 50× objective. The acquisition time of 10 s per frame and two accumulations were used to improve signal-to-noise ratio.

Optical absorption spectra of cut stones in the region (400–750 nm) were measured with the GL Gem SpectrometerTM at room temperature. Both Raman and UV/Vis/NIR spectra were processed in PeakFit 4.1.12 software (Systat Software, Inc. San Jose, CA, USA). Raman and absorption bands were fitted by Lorentz function with the automatic background correction and Savitsky–Golay smoothing.

4. Results

Yellow apatite from Muránska Dlhá Lúka usually forms euhedral to subhedral crystals up to 3 cm in size. It has thick hexagonal prismatic habitus, often enclosed by pinacoid and rarely also pyramidal faces. In some samples, apatite forms long aggregates of subhedral, partly rounded crystals with an area of a few cm^2 . Five apatite crystals with eligible gemological properties were cut as gemstones (Figure 4). Their properties including type of cut, weight and size are listed in the Table 1.

Table 1. Description of the five studied apatite cut stones.

Stone	Shape of Cut	Type of Cut	Dimensions (mm)	Weight (ct)
1	Square	Step cut	6.50 × 5.74 × 4.00	1.34
2	Rectangle	Step cut	8.61 × 6.39 × 4.53	2.25
3	Square	Step cut	4.98 × 4.41 × 3.47	0.68
4	Round	Brilliant	4.60 × 4.46 × 2.89	0.36
5	Round	Brilliant	4.64 × 4.56 × 3.73	0.48

4.1. The Chemical Composition of Hydroxylapatite

The studied apatite has a composition of hydroxylapatite with F^- varying between 0.29 and 0.34 apfu (atoms per formula unit) and Cl^- in range of 0.02–0.05 apfu (Table 1). Calculated OH^- content is dominant, varying between 0.62–0.68 apfu. At the tetrahedral site, only up to 0.003 apfu of both As^{5+} and Si^{4+} substitute for P^{5+} . Calcium is substituted only by small amount of Na (up to 0.006 apfu), Fe^{2+} (up to 0.005 apfu), Mn^{2+} (up to 0.006 apfu), and REE (in total up to 0.017 apfu). The presence of REE is systematic in the whole crystal which does not manifest any significant zoning as indicated by a small chemical variability in the linear profile of 10 analyses measured from the rim to the center of the measured crystal (Figure 5, Table 2).

As suggested by the EMPA data, REE are the most dominant trace elements, especially Y (1011–1087 ppm) (Table 3). From lanthanoids, Nd (360–409 ppm) prevails over Ce (342–376 ppm), Dy (178–190 ppm), Gd (164–178 ppm), Er (124–142 ppm), Sm (125–130 ppm) and Yb (98–113 ppm). Remaining REE are below 100 ppm. Relatively high contents were observed also for Mn (645–706 ppm) and Sr (582–600 ppm) and partly also Zn (9–54 ppm). From light elements, only small amount of Li (1–9 ppm) was detected.

Measured LA-ICP-MS REE contents allowed us to compare them to the chondrite values [37]. This revealed a strong negative Eu anomaly ($\text{Eu}/\text{Eu}^* = 0.082\text{--}0.088$) and slight depletion in the light REE almost without slope with $(\text{Ce}/\text{Yb})_{\text{cn}}$ between 0.93 and 0.98 (Figure 6).

Table 2. Electron microprobe analyses of hydroxylapatite, first provided in wt.% of elements (<DL—content below the detection limit of respective element) and then recalculated on a basis of eight cations.

Sample	1	2	3	4	5	6	7	8	9	10
SO ₃	0.02	<DL	<DL	<DL	<DL	0.01	<DL	<DL	<DL	<DL
P ₂ O ₅	43.0	42.63	42.15	41.31	42.90	42.83	42.90	43.14	42.35	42.35
As ₂ O ₅	<DL	<DL	<DL	<DL	<DL	0.01	0.02	0.03	0.07	0.05
SiO ₂	0.02	0.04	<DL	<DL	0.01	<DL	<DL	0.01	0.01	0.02
TiO ₂	0.10	0.06	0.08	<DL	0.07	<DL	0.04	<DL	<DL	<DL
ThO ₂	<DL	0.03	0.01	0.01	0.02	<DL	0.02	0.02	<DL	<DL
UO ₂	0.04	0.02	<DL	<DL	<DL	<DL	<DL	<DL	0.03	0.02
Al ₂ O ₃	<DL	<DL	0.01	0.01	<DL	<DL	<DL	0.01	<DL	<DL
V ₂ O ₃	<DL	0.04	0.11	0.01	0.06	<DL	<DL	0.08	<DL	<DL
Y ₂ O ₃	0.05	0.13	0.12	0.08	0.03	0.07	0.05	0.06	0.07	0.10
La ₂ O ₃	<DL	0.06	0.02	<DL	<DL	0.06	<DL	<DL	0.01	0.04
Ce ₂ O ₃	0.05	0.08	0.01	0.01	0.06	0.05	0.04	0.05	0.03	0.05
Pr ₂ O ₃	<DL	0.05	0.10	<DL	0.12	<DL	0.01	<DL	0.01	0.11
Nd ₂ O ₃	0.03	<DL	<DL	0.02	0.04	0.05	0.03	<DL	0.04	<DL
Sm ₂ O ₃	<DL	<DL	<DL	<DL	0.09	0.12	<DL	<DL	0.02	0.03
Eu ₂ O ₃	0.04	0.02	<DL	0.05	0.04	0.01	<DL	0.02	<DL	<DL
Gd ₂ O ₃	0.10	0.02	0.09	0.09	0.05	0.01	0.04	0.15	0.01	<DL
Tb ₂ O ₃	0.03	<DL	0.03	<DL	<DL	<DL	<DL	<DL	0.01	0.02
Dy ₂ O ₃	<DL	<DL	0.07	<DL	<DL	0.06	<DL	0.01	<DL	0.15
Ho ₂ O ₃	0.01	<DL	<DL	0.04	<DL	0.03	0.03	<DL	<DL	<DL
Er ₂ O ₃	0.02	<DL	<DL	0.02	<DL	<DL	0.07	0.05	0.01	<DL
Tm ₂ O ₃	<DL									
Yb ₂ O ₃	<DL	<DL	0.06	0.02	<DL	0.04	0.02	0.03	0.03	0.03
Lu ₂ O ₃	<DL	<DL	0.03	<DL	0.06	0.07	<DL	0.09	0.06	0.01
FeO	0.07	0.05	0.02	0.04	0.04	0.05	0.04	<DL	0.07	<DL
MnO	0.01	<DL	0.04	<DL	0.04	0.05	0.05	0.07	0.08	0.07
CaO	54.95	55.12	55.20	55.09	54.89	55.11	55.11	55.22	55.25	55.13
PbO	0.05	<DL	<DL	0.01	<DL	<DL	0.06	<DL	<DL	0.01
Na ₂ O	0.03	0.03	0.02	0.02	0.04	0.04	0.02	0.04	<DL	0.03
F	1.11	1.27	1.11	1.19	1.17	1.20	1.15	1.19	1.19	1.21
Cl	0.36	0.33	0.37	0.18	0.34	0.21	0.15	0.18	0.37	0.31
H ₂ O	1.18	1.10	1.16	1.16	1.15	1.17	1.21	1.19	1.13	1.13
O = F	−0.56	−0.64	−0.56	−0.59	−0.58	−0.60	−0.57	−0.60	−0.59	−0.61
O = Cl	−0.18	−0.16	−0.19	−0.09	−0.17	−0.11	−0.07	−0.09	−0.18	−0.16
Total	99.38	99.15	98.88	97.49	99.30	99.37	99.20	99.75	98.94	98.98
S	0.001	-	-	-	-	0.001	-	-	-	-
P	3.047	3.023	2.997	2.970	3.040	3.032	3.037	3.041	3.008	3.010
As	-	-	-	-	-	-	0.001	0.001	0.003	0.002
Si	0.002	0.003	-	-	0.001	-	-	-	0.001	0.002
Σ	3.050	3.026	2.997	2.970	3.041	3.033	3.039	3.043	3.013	3.013
Ti	0.006	0.004	0.005	-	0.004	-	0.002	-	-	-
Th	-	0.001	-	-	-	-	-	-	-	-
U	0.001	-	-	-	-	-	-	-	0.001	-
Al	-	-	-	0.001	-	-	-	0.001	-	-
V	-	0.003	0.008	-	0.004	-	-	0.005	-	-
Y	0.002	0.006	0.005	0.003	0.002	0.003	0.002	0.003	0.003	0.004
La	-	0.002	-	-	-	0.002	-	-	-	0.001
Ce	0.001	0.002	-	-	0.002	0.001	0.001	0.001	0.001	0.002
Pr	-	0.002	0.003	-	0.004	-	-	-	-	0.003
Nd	0.001	-	-	0.001	0.001	0.001	0.001	-	0.001	-
Sm	-	-	-	-	0.003	0.004	-	-	0.001	0.001
Eu	0.001	-	-	0.001	0.001	-	-	-	-	-
Gd	0.003	0.001	0.002	0.003	0.001	-	0.001	0.004	-	-
Tb	0.001	-	0.001	-	-	-	-	-	-	-
Dy	-	-	0.002	-	-	0.002	-	-	-	0.004

Table 2. Cont.

Sample	1	2	3	4	5	6	7	8	9	10
Ho	-	-	-	0.001	-	0.001	0.001	-	-	-
Er	0.001	-	-	-	-	-	0.002	0.001	-	-
Tm	-	-	-	-	-	-	-	-	-	-
Yb	-	-	0.001	-	-	0.001	0.001	0.001	0.001	0.001
Lu	-	-	0.001	-	0.001	0.002	-	0.002	0.001	-
Fe	0.005	0.003	0.001	0.003	0.002	0.003	0.003	-	0.005	-
Mn	0.001	-	0.003	-	0.003	0.003	0.003	0.005	0.006	0.005
Mg	-	-	-	-	-	-	-	-	-	-
Ca	4.922	4.947	4.967	5.012	4.924	4.937	4.939	4.926	4.967	4.959
Pb	0.001	-	-	-	-	-	0.001	-	-	-
Na	0.004	0.004	0.003	0.003	0.006	0.006	0.003	0.006	-	0.005
Σ	4.950	4.974	5.003	5.030	4.959	4.967	4.961	4.957	4.987	4.987
F	0.294	0.336	0.296	0.319	0.310	0.316	0.304	0.314	0.315	0.322
Cl	0.050	0.046	0.053	0.026	0.048	0.030	0.021	0.025	0.052	0.044
OH	0.656	0.617	0.651	0.656	0.642	0.653	0.676	0.660	0.633	0.634
Σ	1.000	1.000	1.000	1.000	1.000	1.000	1.000	1.000	1.000	1.000

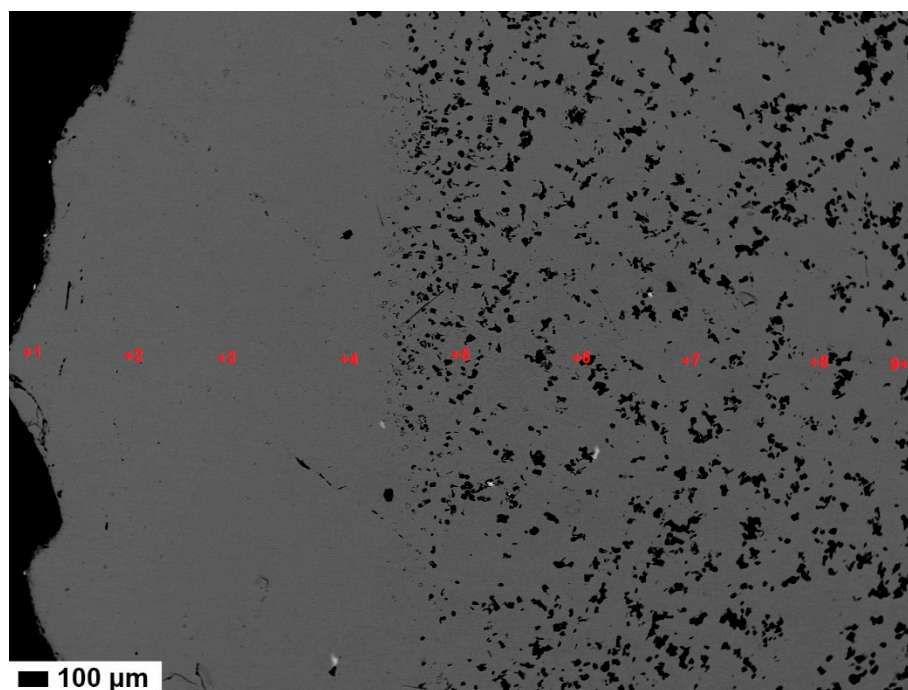


Figure 5. Back-scattered electron image of hydroxylapatite from Muránska Dlhá Lúka with marks and numbers of measured points.

4.2. Spectroscopic Characterization of Hydroxylapatite

Hydroxylapatite was studied by several spectroscopic methods including FTIR, Raman and optical absorption spectroscopy.

FTIR spectrum exhibited absorption bands assigned to $[\text{PO}_4]^{3-}$, $[\text{CO}_3]^{2-}$ and to OH groups (Figure 7, Table 4). The $[\text{PO}_4]^{3-}$ gives several bands that belongs to: (1) bending vibrations ν_2 at 438 and 473 cm^{-1} ; (2) bending vibrations ν_4 within region 572–603 cm^{-1} ; (3) symmetric stretching vibration ν_1 at 962 cm^{-1} ; (4) antisymmetric stretching vibration ν_3 for 1046–1091 cm^{-1} . The $[\text{CO}_3]^{2-}$ bands were attributed to (1) bending vibrations ν_2 at 838 and 894 cm^{-1} ; (2) bending vibrations ν_4 at 668 and 717 cm^{-1} . Stretching $[\text{CO}_3]^{2-}$ vibrations were not detected in the spectra. The OH^- absorption bands occur at 640, 3544, 3568 cm^{-1} . All these bands are in agreement with values published by [38,39].

Table 3. The trace-elements contents (in ppm) in hydroxylapatite from Muránska Dlhá Lúka measured by laser-ablation inductively coupled plasma mass spectrometry (LA-ICP-MS; DL—limit of detection, <DL—content below the detection limit of respective element).

Point	Li	Sc	Ti	Mn	Cu	Zn	Ga	Ge	Sr	Y	Cd	Sb	Ba	Th	U
1	6	0.3	8	645	1.1	54	2	4	600	1042	8	0.66	0.06	7	6
2	9	0.2	5	653	0.4	14	2	4	582	1011	7	0.71	0.07	5	5
3	1	0.2	7	706	<DL	9	3	4	587	1087	10	0.47	0.16	6	6
DL	1	0.1	0.05	0.4	0.1	0.05	0.05	0.79	0.06	0.05	0.47	0.1	0.05	0.05	0.05
Point	La	Ce	Pr	Nd	Sm	Eu	Gd	Tb	Dy	Ho	Er	Tm	Yb	Lu	Pb
1	77	361	64	378	129	4	171	28	190	41	131	18	104	15	27
2	70	342	63	360	125	4	164	25	178	40	124	17	98	14	26
3	79	376	71	409	130	4	178	29	205	46	142	18	113	17	28
DL	0.05	0.05	0.05	0.05	0.05	0.05	0.05	0.05	0.05	0.05	0.05	0.05	0.05	0.05	0.05

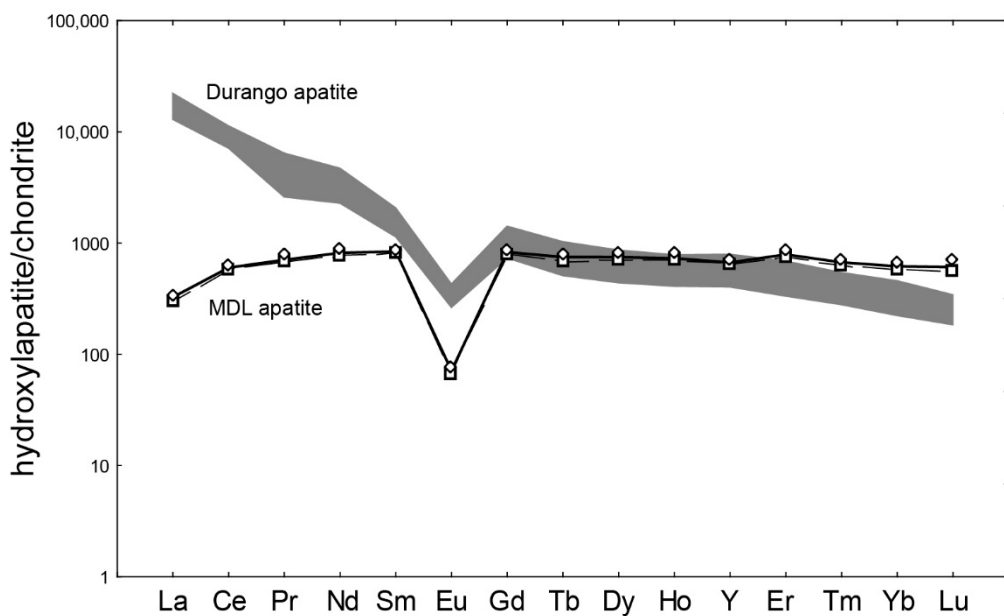


Figure 6. Chondrite-normalized REE patterns of hydroxylapatite from Muránska Dlhá Lúka measured by LA-ICP-MS (normalized on chondrite from [37]).

Table 4. The FTIR spectrum band assignment of hydroxylapatite from Muránska Dlhá Lúka according to [38,39].

Assignment	Wavenumber (cm ⁻¹)
ν_2 [PO ₄] ³⁻ mode	438
ν_2 [PO ₄] ³⁻ mode	473
ν_4 [PO ₄] ³⁻ mode	572
ν_4 [PO ₄] ³⁻ mode	603
OH ⁻ vibration	640
ν_4 [CO ₃] ²⁻ mode (A)	668
ν_4 [CO ₃] ²⁻ mode (B)	717
ν_2 [CO ₃] ²⁻ mode	838
ν_2 [CO ₃] ²⁻ mode	894
ν_1 [PO ₄] ³⁻ mode	962
ν_3 [PO ₄] ³⁻ mode	1046
ν_3 [PO ₄] ³⁻ mode	1091
OH ⁻ vibration	3544
OH ⁻ vibration	3568

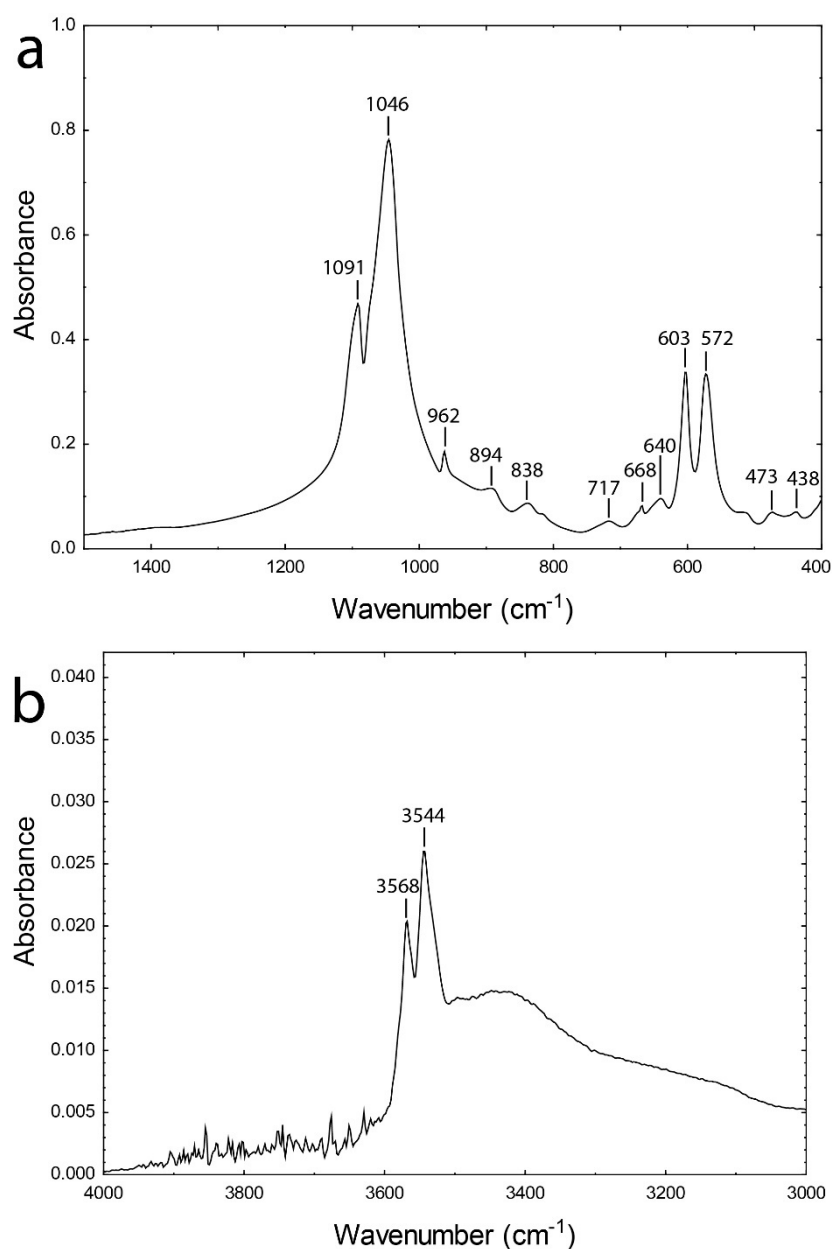


Figure 7. The FTIR spectrum of hydroxylapatite from Muránska Dlhá Lúka. (a) 400–1500 cm^{-1} ; (b) 3000–4000 cm^{-1} .

The Raman spectrum of MDL apatite (Figure 8) revealed that lattice, $[\text{PO}_4]^{3-}$ and $[\text{CO}_3]^{2-}$ modes were detected (Table 5). The Ca- $[\text{PO}_4]^{3-}$ lattice modes were identified below 300 cm^{-1} . The $[\text{PO}_4]^{3-}$ modes were assigned to (1) bending vibrations ν_2 in the range of 430 and 450 cm^{-1} ; (2) bending vibrations ν_4 are between 570–620 cm^{-1} ; (3) the most intensive band of symmetric stretching vibration ν_1 at 962 cm^{-1} . The bands between 1020–1080 cm^{-1} can be attributed either to antisymmetric stretching vibration ν_3 of $[\text{PO}_4]^{3-}$ or symmetric stretching vibrations ν_1 of B-type substituted $[\text{CO}_3]^{2-}$. The OH^- vibrations were not observed. All these bands are in agreement with values published by [39,40].

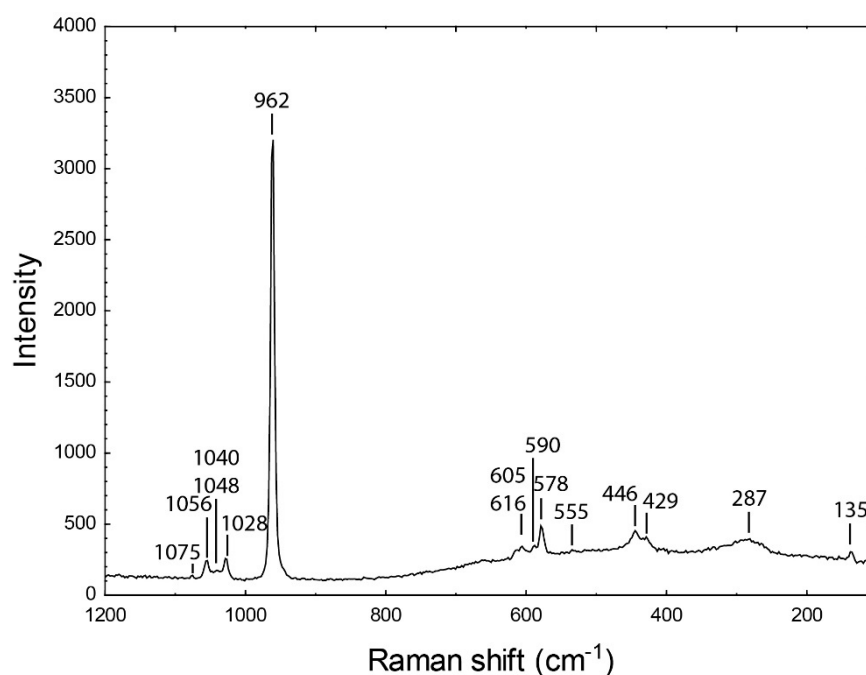


Figure 8. Raman spectrum of hydroxylapatite from Muránska Dlhá Lúka measured with blue laser.

Table 5. Raman spectrum band assignment of hydroxylapatite from Muránska Dlhá Lúka.

Assignment	Symmetry	Raman Shift (cm ⁻¹)
Lattice mode	E _{1g}	135
Lattice mode *	E _{1g}	287
ν ₂ [PO ₄] ³⁻ mode	E _{1g}	429
ν ₂ [PO ₄] ³⁻ mode	E _{2g}	446
ν ₄ [PO ₄] ³⁻ mode	2E _{2g}	578
ν ₄ [PO ₄] ³⁻ mode	E _{1g}	590
ν ₄ [PO ₄] ³⁻ mode	2A _g	605
ν ₄ [PO ₄] ³⁻ mode	2E _{2g}	616
ν ₁ [PO ₄] ³⁻ mode	A _g	962
ν ₃ [PO ₄] ³⁻ mode	2E _{2g}	1028
ν ₃ [PO ₄] ³⁻ mode	E _{1g}	1040
ν ₃ [PO ₄] ³⁻ mode	2A _g	1048
ν ₃ [PO ₄] ³⁻ mode	2E _{2g}	1056
ν ₁ [CO ₃] ²⁻ B mode		1075

* Possible luminescence.

The photoluminescence spectrum of MDL hydroxylapatite was measured with 473 nm laser light source (Figure 9, Table 6). It shows prominent luminescence features between 550 and 620 nm attributed to Dy³⁺, Sm³⁺ and Pr³⁺. Moreover, there could also be a Mn²⁺ luminescence band at around 570 nm but it cannot be clearly resolved. This corresponds to the yellow region of the visible light. Another luminescence bands are in the red and infrared region –640–655 and 700–715 nm of Sm³⁺, 752 nm of Dy³⁺ and 860–880 nm of Nd³⁺. A photoluminescence measurement with the UV-light source (266 nm) was also attempted and provided a prominent band centered at 360 nm but was distorted due to the interference effects. This band can be attributed to Ce³⁺.

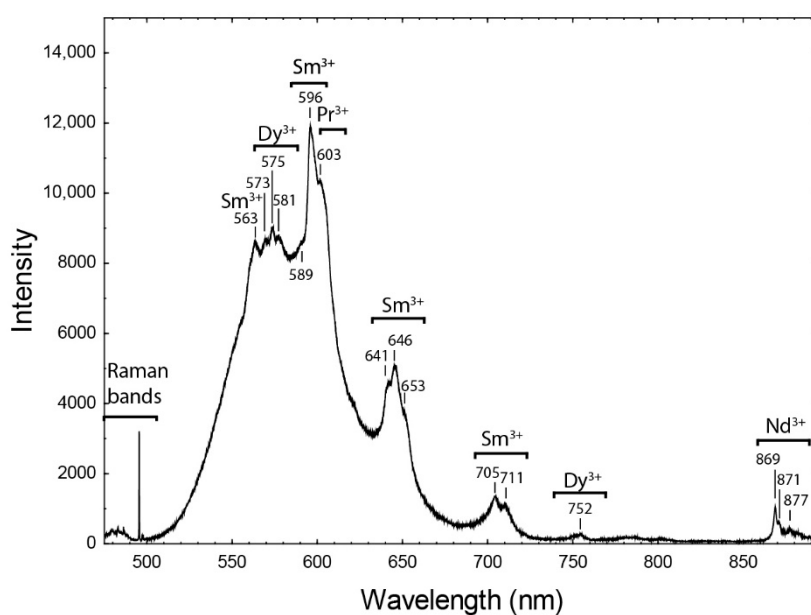


Figure 9. The luminescence spectrum of hydroxylapatite from Muránska Dlhá Lúka measured with blue laser on the Raman spectrometer.

Table 6. The luminescence spectrum band assignment of hydroxylapatite from Muránska Dlhá Lúka.

Assignment	Electron Transition	Reference	Wavelength (nm)
Sm ³⁺	⁴ G _{5/2} - ⁶ H _{5/2}	[41]	563
Dy ³⁺	⁵ D ₀ - ⁷ F ₀	[41]	573
Dy ³⁺	⁵ D ₀ - ⁷ F ₀	[41]	575
Dy ³⁺	⁵ D ₀ - ⁷ F ₀	[41]	581
Sm ³⁺	⁴ G _{5/2} - ⁶ H _{7/2}	[41]	589
Sm ³⁺	⁴ G _{5/2} - ⁶ H _{7/2}	[41]	596
Pr ³⁺	¹ D ₂ - ³ H ₄	[41]	603
Sm ³⁺	⁴ G _{5/2} - ⁶ H _{9/2}	[42]	641
Sm ³⁺	⁴ G _{5/2} - ⁶ H _{9/2}	[42]	646
Sm ³⁺	⁴ G _{5/2} - ⁶ H _{9/2}	[42]	653
Sm ³⁺	⁴ G _{5/2} - ⁶ H _{11/2}	[42]	705
Sm ³⁺	⁴ G _{5/2} - ⁶ H _{11/2}	[42]	711
Dy ³⁺	⁴ F _{9/2} - ⁶ H _{9/2}	[41]	752
Nd ³⁺	⁴ F _{3/2} - ⁴ I _{9/2}	[41]	869
Nd ³⁺	⁴ F _{3/2} - ⁴ I _{9/2}	[41]	871
Nd ³⁺	⁴ F _{3/2} - ⁴ I _{9/2}	[41]	877

The optical absorption spectra of three cut stones (Figure 10, Table 7) show many similarities. All samples display either an intensive band in the UV region or an absorption edge. However, the range of the light source did not allow proper measurement in this region. In the visible region, the most prominent are 585–590 nm bands attributed to Nd³⁺ and wide absorption region between 600 and 800 nm which was resolved to three possible bands of Mn²⁺ (626–630 nm), Ce³⁺-SiO³⁻ photochromic center (675–680 nm) and Nd³⁺ (626–630 nm).

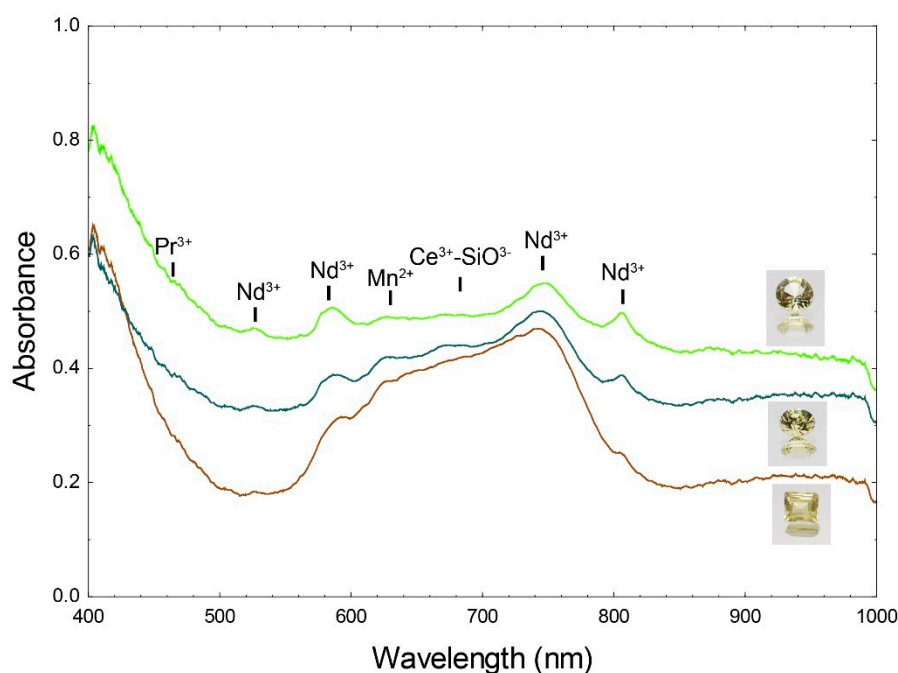


Figure 10. Optical absorption spectrum of hydroxylapatite cut stones from Muránska Dlhá Lúka.

Table 7. The optical spectral bands (in nm) of the hydroxylapatite cut stones from Muránska Dlhá Lúka.

Sample			Assignment	Process	State	Reference
3	4	5				
-	457	457	Pr ³⁺	4f–5d transition	³ P ₀	[43]
526	526	526	Nd ³⁺	4f–5d transition	⁴ G _{7/2}	[43]
590	585	587	Nd ³⁺	4f–5d transition	⁴ G _{5/2} , ⁴ G _{7/2}	[43]
626	630	630	Mn ²⁺	4d–4d transition	⁴ T _{1g}	[44]
675	680	676	Ce ³⁺ -SiO ³⁻	photochromic center		[45]
740	747	744	Nd ³⁺	4f–5d transition	⁴ F _{7/2}	[43]
805	805	801	Nd ³⁺	4f–5d transition	⁴ F _{5/2}	[43]

5. Discussion and Conclusions

5.1. Crystal Chemistry of Hydroxylapatite from Muránska Dlhá Lúka

Apatite from Muránska Dlhá Lúka is the solid solution of hydroxylapatite and fluorapatite but the F content is always below 0.33 apfu. Although the OH content was not quantified, its presence was evidenced by the presence of O-H bands in the FTIR spectrum. The [CO₃]²⁻ groups could also be partly substituting at the anionic site as discussed later, but the overall composition does not suggest that this substitution could have any larger impact on the hydroxylapatite classification. In terms of cationic composition, studied hydroxylapatite is close to the end-member composition, only REE (including Y), Fe, Mn and Na are in concentrations measurable by EMPA. LA-ICP-MS data confirmed that only Y has content higher than 1000 ppm; Mn, Sr and some REE vary between 100–1000 ppm. Consequently, possible substitutions are limited on these elements.

Manganese and iron can substitute for Ca²⁺ relatively easy in the homovalent substitution. The interpretation of REE incorporation into the apatite structure requires determination of their position in the structure and their charge-balancing. Based on the similar ionic radii, REE substitute for Ca in apatite. There are two distinct Ca sites in the apatite structure: (1) Ca1, site symmetry 3, coordination 9, CaO₉ polyhedron; (2) Ca2, site symmetry *m*, coordination 7, CaO₆A (A = F, OH, Cl) polyhedron [46]. The site preference of REE in apatite can be determined by the bond valences at

specific sites [47–49]. Ca2 is coordinated by the volatile anion (F, OH, Cl) and is underbonded in endmember fluorapatite which suggests that minor amounts of trivalent REE should favor Ca2 over Ca1, to increase the bond valences of both Ca2 and F, and Na should then favor Ca1 [49]. However, if REE are not treated as a uniform group of elements, bond valence calculations revealed that HREE (Gd–Lu) are underbonded in either Ca sites, whereas, La, Ce, and Pr are slightly overbonded in the Ca1 site and, therefore, should prefer Ca2, Pm and Sm should favor Ca1, and Nd should readily substitute into either Ca1 or Ca2 [47]. Consequently, LREE in fluorapatite may not behave as a chemically coherent group during substitution and their distribution coefficients display a generally concave downward pattern centered on Nd [47]. Consequently, we presume that REE in studied apatite occupy Ca2 site, predominantly.

Four main types of charge-balancing mechanisms have been proposed for the substitution of Ca^{2+} by REE^{3+} (and Y^{3+}) in apatites: (1) $\text{REE}^{3+} + \text{X}^{2-} = \text{Ca}^{2+} + \text{F}^-$ ($\text{X} = \text{O}, \text{S}$); (2) $\text{REE}^{3+} + \text{M}^+ = 2 \text{Ca}^{2+}$ ($\text{M} = \text{Na}, \text{K}$); (3) $\text{REE}^{3+} + [\text{SiO}_4]^{4-} = \text{Ca}^{2+} + [\text{PO}_4]^{3-}$; (4) $2 \text{REE}^{3+} + \square$ (vacancy) = 3Ca^{2+} [49–58]. Based on the chemical composition data of MDL hydroxylapatite, two substitutions can be tested: (1) $\text{REE}^{3+} + [\text{SiO}_4]^{4-} = \text{Ca}^{2+} + [\text{PO}_4]^{3-}$ (vector $\text{REE}^{3+}\text{Si}^{4+}(\text{Ca}^{2+}\text{P}^{5+})_{-1}$) and (2) $\text{REE}^{3+} + \text{Na}^+ = 2 \text{Ca}^{2+}$ (vector $\text{REE}^{3+}\text{Na}^+(\text{Ca}^{2+})_{-2}$) (Figure 11). Both substitutions are possible in the studied sample, but they seem to be insufficient to charge-balance the bulk REEs content. If Ca + P is compared to Si + REE (Figure 11a), studied sample follows the vector of $\text{REE}^{3+}\text{Na}^+(\text{Ca}^{2+})_{-2}$ substitution. However, straight comparison of Na + REE to Ca indicates that Na content is also lower than REE^{3+} content. Consequently, another substitution mechanism should be involved.

The $2 \text{REE}^{3+} + \square$ (vacancy) = 3Ca^{2+} substitution cannot be verified without the structural refinement data. However, the slightly lower Ca-sites sum suggests that this substitution is not impossible. The $\text{REE}^{3+} + \text{X}^{2-} = \text{Ca}^{2+} + \text{F}^-$ substitution involves divalent anion, e.g., O^{2-} [50,59,60] or S^{2-} [61,62]. However, there are no indications of increased S content and the presence of O substituting for OH cannot be determined with the current data.

Interestingly, the presence of $[\text{CO}_3]^{2-}$ modes in the FTIR and Raman spectrum of studied samples indicate that $[\text{CO}_3]^{2-}$ could also be involved in the charge-balancing of REEs. A $[\text{CO}_3]^{2-}$ ion can substitute at two different sites in apatite: (1) the OH ion site (channel site) called A site and (2) the PO_4 site called B site. The FTIR data of studied hydroxylapatite indicate a possible presence of both types of substitution.

In synthetic apatites with A-site carbonate group, the incorporation of $[\text{CO}_3]^{2-}$ ions into the c-axis anion channels has been shown to follow $[\text{CO}_3]^{2-} + \square = 2 \text{F}^-$ substitution [63,64]. Polarized IR studies [3] suggested that the planar $[\text{CO}_3]^{2-}$ ions in the anion channels are oriented approximately parallel to the c-axis to minimize the steric strain related to the incorporation of this large ion [65]. This configuration has been confirmed by single-crystal X-ray structure refinement of a flux-grown, apatite with A-site carbonate [66].

Structural mechanism of B-site $[\text{CO}_3]^{2-}$ substitution surely results in a structural rearrangement due to the different geometry of substituting groups [67]. The first possibility is to place a carbon atom exactly at the phosphorus position with the same coordinates [68]. However, it would result in unacceptably large C–O distances, an impossible geometry of the $[\text{CO}_3]^{2-}$ polyhedron with C outside the plane defined by the three coordinating oxygens and the bond-valence unbalance at the fourth oxygen not bonded to C [67].

Published polarized IR spectroscopy data revealed that planes of $[\text{CO}_3]^{2-}$ triangles are oblique to the c axis in the angle of $37 \pm 4^\circ$ and likely occupy the sloping faces of the tetrahedra [3]. Therefore, incorporation of C requires larger structural deformations. The carbonate triangles may occupy any of the tetrahedral faces but in each specific case they seem to stick to a certain face(s). There can be two preferred orientations of $[\text{CO}_3]^{2-}$ triangles sharing one of their edges distributed randomly in the structure [69]. The charge unbalance resulting from the $[\text{CO}_3]^{2-}$ for $(\text{PO}_4)^{3-}$ substitution is primarily compensated by vacancies at the Ca1 sites [69]. However, the B carbonate ion can be also located near the sloping faces of the substituted phosphate group but inclined at an angle of 53° to the

mirror plane [70]. One of the O3 O atoms of the phosphate group is displaced to O8 and the second, symmetrically related O3 is lost to maintain charge balance. The O1 atom is displaced slightly to O9 and the third B carbonate O atom is concealed by the electron density of O2. The charge unbalance of the substitution is here compensated by Na substituting for Ca [70].

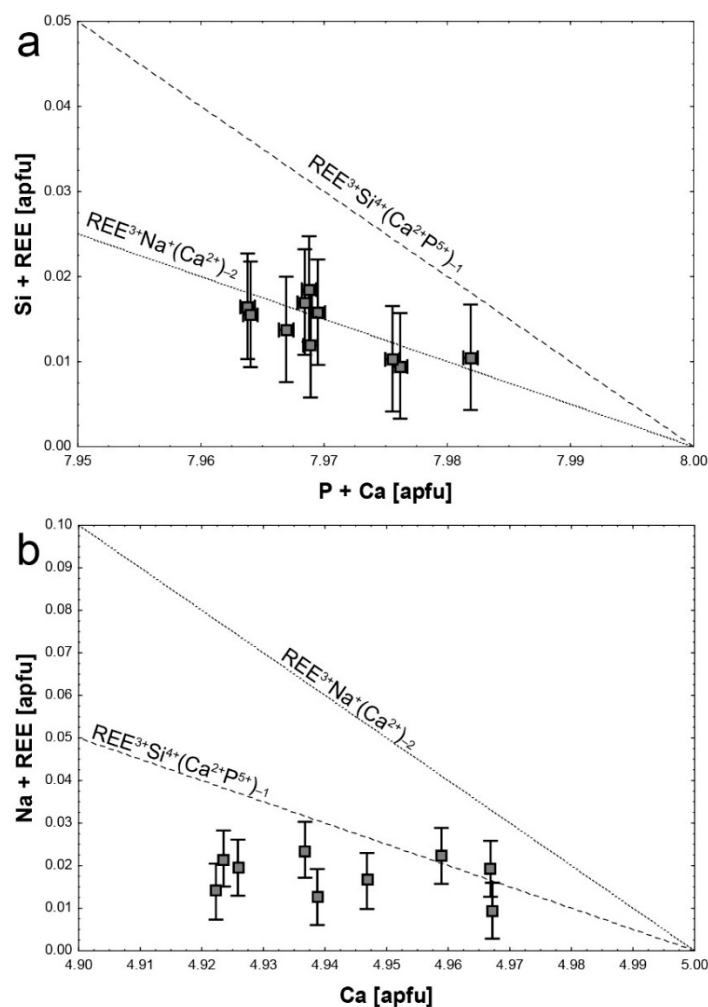


Figure 11. Substitution diagram of hydroxylapatite from Muránska Dlhá Lúka (data points with error bars): (a) Ca + P vs. Si + REE; (b) Ca vs. Na + REE. Dashes and dotted lines represent ideal trend of specified substitutions.

In the studied hydroxylapatite, Na content is small, vacancies cannot be determined but REE content is too high to be charge-balanced by Na^+ for Ca^{2+} or Si^{4+} for P^{5+} . Consequently, two substitutions involving REE and $[CO_3]^{2-}$ can be proposed: (1) $REE^{3+} + {}^A[CO_3]^{2-} = Ca^{2+} + F^-$ and (2) $REE^{3+} + \square + {}^B[CO_3]^{2-} = 2 Ca^{2+} + {}^B[PO_4]^{3-}$ substitution. The first substitution is only the variation of $REE^{3+} + X^{2-} = Ca^{2+} + F^-$ substitution, where the X anion is $[CO_3]^{2-}$ group. However, due to the local structural requirements, A and B carbonate ions have to be paired because the off-axis oxygen (O5) of the type A carbonate is pushed too close to an O3 oxygen of the phosphate group in the average structure. In the local structure, O3 is either displaced to O8 or removed from the structure and the Na cation helps to charge balance the oxygen vacancy [71]. Consequently, the structural accommodation of the $[CO_3]^{2-}$ substitutions requires local coupling of Na cation and both channel (type A) and phosphate (type B) carbonate ion defects [70,71]. In the Na deficiency and the excess of REE, the final composition can result from coupling of both substitution mechanisms with $(REE^{3+} + \square)$ charge-balancing $[CO_3]^{2-}$ groups instead of $(Ca^{2+} + Na^+)$ resulting in the theoretical $Ca_8REE\square[(PO_4)_5]$

(CO₃)](CO₃) end-member composition. The possibility of this complex substitution mechanism cannot, however, be verified on the studied sample by the structural refinement due to a low content of REE and likely also C. However, it is supported by the presence of both A and B carbonate ion bands in the FTIR and Raman spectra, the low Na content and the excess of REE.

5.2. Genetical Conditions of Hydroxylapatite from Muránska Dlhá Lúka

The genetical conditions, source of fluids and influence of the host environment can be derived from the trace element composition of apatite. REE are very useful tracers of genetical conditions as well as elements reflecting fractionation of rocks such as Sr and Mn.

Chondrite-normalized REE patterns in apatite typically have negative slopes, indicating substantial relative enrichment in the LREE [49,72]. Moreover, the slope of chondrite-normalized patterns increases from highly fractionated rock types to mafic less-fractionated rocks. Therefore, the chondrite-normalized (Ce/Yb)_{cn} ratio is over 100 in apatites from ultramafic rocks, but apatites from granitoid rocks rarely show (Ce/Yb)_{cn} values higher than 15–20. In apatites from granitic pegmatites, it is even lower—below 1, indicating heavy REE enrichment and light REE depletion [2].

The Eu anomaly in chondrite-normalized REE patterns is also indicative of apatite genetical condition. Apatites from mantle-derived lherzolites and carbonatites display weak negative Eu anomalies with Eu/Eu* values between 0.7–1. More pronounced negative Eu anomalies are usually found in pegmatitic apatites with Eu/Eu* of 0.25 to 0.04. Apatites from granitoids have the lowest Eu anomalies, with Eu/Eu* ratios attaining 0.01–0.06 and 0.4 in average [2]. The amplitude of Eu anomalies in apatites increases from less to more fractionated rocks and probably is controlled by the crystallization of feldspars, which concentrate Eu²⁺ from the melt; K-feldspar shows a stronger preference for Eu than plagioclase [73].

Strontium, yttrium, and manganese are very useful for determination of the apatite origin due to the large variations in concentrations depending on their genetical conditions. Strontium concentrations vary from less than 50 ppm to over several thousand ppm [2]. It may reach percentage levels in apatites from mantle-derived lherzolite xenoliths [74]. In contrast, the lowest Sr contents are found in apatites from highly fractionated granitoids and granitic pegmatites (less than 100 ppm) [2]. Yttrium concentration ranges from tens of ppm to over 1% with the highest concentrations found in apatites from granitic pegmatites, while the lowest are found in carbonatites and lherzolites [2]. Manganese contents are also extremely variable, varying from less than 100 ppm to several thousand ppm, rarely reaching the percentage level. The lowest values (100–300 ppm) were found in apatites from carbonatites and the Kiruna iron ore deposit, while the highest Mn values (0.1–1 wt.%) are in apatites from granite pegmatites and highly fractionated granites [2].

Plots of Sr versus Y and Mn, (Ce/Yb)_{cn} versus the sum of REE, and Y against Eu/Eu* (Figure 12) allow the clearest definition of fields of apatite compositions for rock types of contrasting composition [2]. However, their use in hydrothermal apatite is limited and should be used to determine possible sources of fluids and impact of the vein host rock. The impact of ultrabasic host rock—serpentinite—can be visible on the Sr concentrations. In both plots with Sr, the studied apatite reflects an affinity to basic to ultrabasic rocks (Figure 12a,b). However, the Y and Mn concentrations are relatively higher, closer to granitic rocks, and consequently, MDL hydroxylapatite is shifted into or to the close vicinity of exotic alkaline rocks—jacupirangite and larvikites. The chondrite-normalized patterns of the studied are typical for granitic rocks and their pegmatites in terms of the slope of the pattern as well as Eu anomaly (Figure 12c,d). This is also supported by the presence of Li at measurable concentrations. The yellow REE³⁺ (±Mn²⁺)-induced photoluminescence is also typical feature of granitoid-related apatites [75,76].

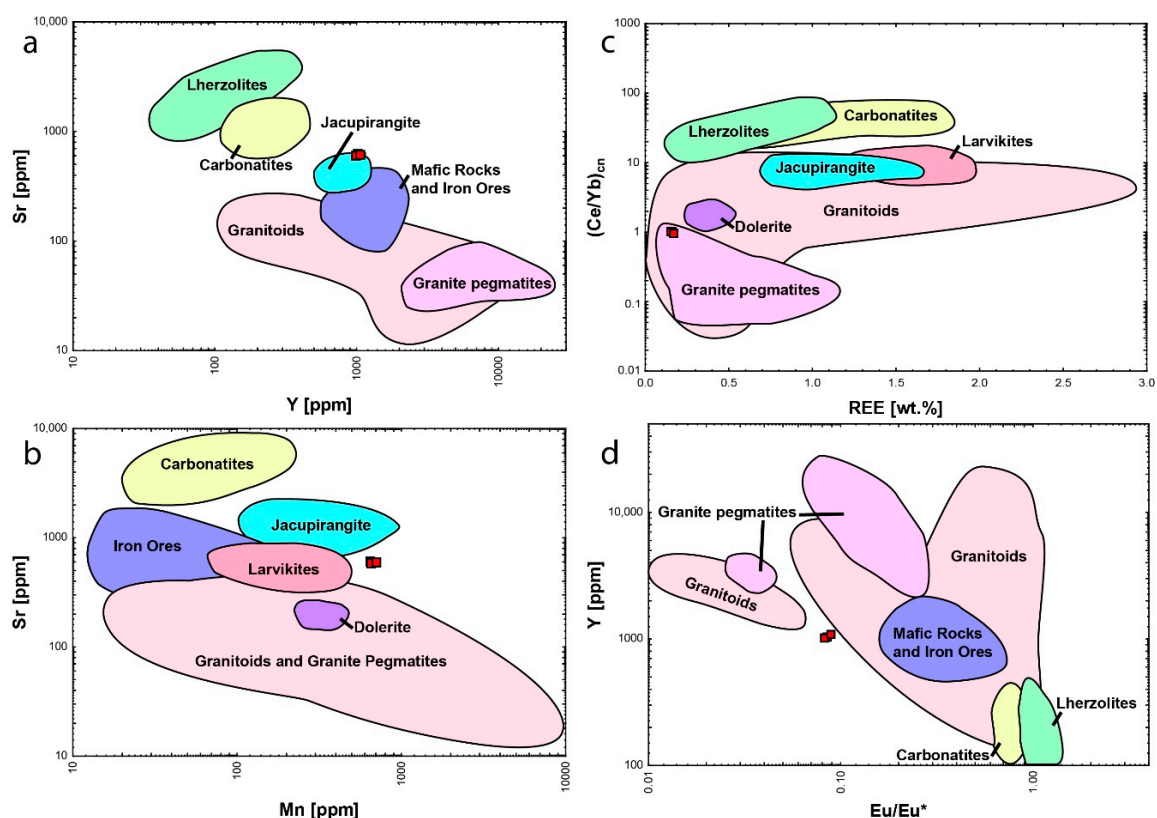


Figure 12. The Muránska Dlhá Lúka hydroxylapatite compositions (red squares) in plots of Sr versus (a) Y and (b) Mn, (c) (Ce/Yb)_{cn} versus the sum of REE, and (d) Y against Eu/Eu* with fields of apatite compositions for selected rock types [1].

Consequently, we can assume that hydroxylapatite from Muránska Dlhá Lúka formed from fluids derived from (meta) granitic rocks as evidenced by the chondrite-normalized REE patterns and Mn and Y concentrations. Fluids enriched in P and with REE, Y, Mn and Li were likely derived from Muráň complex orthogneisses by the Alpine deformation and recrystallization in greenschist to lower amphibolite facies at 500–530 °C and 8–9 kbar [27,77]. In the Hnúšť'a-Mútnik carbonate-talc deposit, similar mineralization with apatite, tourmaline, diopside, phlogopite and amphiboles developed at metamorphic processes with an intensive fluid regime 550–600 °C and 7–9 kbars [78]. However, in Muránska Dlhá Lúka, the apatite trace-elements composition documents extensive fluid regime with a mutual impact of fluid source and host rock.

5.3. Gemological Properties of Hydroxylapatite from Muránska Dlhá Lúka

Since hydroxylapatite from Muránska Dlhá Lúka very often forms euhedral semitransparent to transparent crystals which can be cut, it can be used as gemological material. Therefore, its importance for gemological purposes can be established. With its striking, almost golden yellow color caused mainly by REE, it bears a resemblance with famous Durango apatites. Therefore, the mutual comparison of their chemical and spectroscopic properties can be useful.

Trace-elements composition can be used as discrimination factor for determination of the stone source. Comparison of MDL and Durango apatites (LA-ICP-MS data from [79]) revealed that apatites from both localities contain Mn, Sr, Y and REE, but there are differences in the concentration of these elements and also presence of other elements. Durango apatite is generally richer in REE with La and Ce exceeding 5000 ppm and Nd up to 2200 ppm in order of Ce > La >> Nd. The REE content in MDL apatite is around ten times lower than Durango with Nd > Ce >> La. There is also a significant difference in the slope of chondrite-normalized patterns of REE and Eu anomaly between

both localities. Durango apatite is significantly more LREE dominant with $(Ce/Yb)_{cn}$ of up to 30 and has smaller Eu anomaly ($Eu/Eu^* = 0.082\text{--}0.088$), while the MDL apatite has almost horizontal slope of chondrite-normalized REE pattern with $(Ce/Yb)_{cn}$ of 0.93 and 0.98 and larger negative Eu anomaly ($Eu/Eu^* = 0.082\text{--}0.088$). The MDL apatite is richer in Mn (647–706 ppm in MDL, 33–445 ppm in Durango), Pb (26–28 ppm in MDL, up to 4.4 ppm in Durango) and Li (1–9 ppm in MDL, below the detection limit in Durango). In contrast, Durango apatite is more enriched in As (below the detection limit in MDL, 416–1261 ppm in Durango), V (below the detection limit in MDL, 24–52 ppm in Durango), Th (5–7 ppm in MDL, 195–457 ppm in Durango) and U (5–6 ppm in MDL, 9–23 ppm in Durango) than MDL sample. The concentrations of Sr (582–600 ppm in MDL, 440–618 ppm in Durango) and Y (1011–1087 ppm in MDL, 624–1233 ppm in Durango) are similar in both apatites. Consequently, trace element compositions are a very useful tool for distinguishing source localities of yellow gemstone quality apatites colored by REE.

The yellow color is a very intriguing and attractive feature of MDL apatite. However, the optical spectra of the three cut stones do not indicate any significant absorption bands generating yellow color by limiting transmission in the neighboring regions of visible light. This is very similar to optical absorption spectrum of Durango apatite [80]. However, MDL apatite display relatively strong $REE^{3+}(\pm Mn^{2+})$ -induced photoluminescence at 550 and 620 nm with the maximum straight in the yellow color region which can be induced even by the blue 432 nm light. Consequently, the final color of MDL apatite appearing gold-yellow in sunlight can result from transmission in the green-yellow region but is strongly enhanced by yellow luminescence induced by the UV to blue light.

Author Contributions: Concept of study, P.B.; Field research and sample collection T.B., P.S.; methodology, P.B., J.F., J.Š., L.I., H.P., R.Š., T.M., S.M., T.V.; formal investigation, P.B., J.F., J.Š., L.I.; compilation and writing of the manuscript, P.B., J.F., T.B.; review and editing of manuscript, P.B. All authors have read and agreed to the published version of the manuscript.

Funding: This research was funded by the Slovak Research and Development Agency under the Contract, number APVV-18-0065 (P.B., J.F.) and by the Ministry of Education of Slovak Republic grant agency under the contracts VEGA-1/0137/20 (P.B., J.F.) and VEGA 2/0028/20 (T.M.).

Acknowledgments: We are indebted to Michal Krupa for finding and identification of apatite as a new mineral on the Muránska Dlhá Lúka locality. We are also grateful to Zuzana Pulišová for cutting gemstones. Last, but not least, we thank editor and reviewers for their detailed reviews which improved the quality of our work.

Conflicts of Interest: The authors declare no conflict of interest.

References

1. Pasero, M.; Kampf, A.R.; Ferraris, C.; Pekov, I.V.; Rakovan, J.; White, T.J. Nomenclature of the apatite supergroup minerals. *Eur. J. Mineral.* **2010**, *22*, 163–179. [[CrossRef](#)]
2. Belousova, E.A.; Griffin, W.L.; O'Reilly, S.Y.; Fisher, N.I. Apatite as an indicator mineral for mineral exploration: Trace-element compositions and their relationship to host rock type. *J. Geochem. Explor.* **2002**, *76*, 45–69. [[CrossRef](#)]
3. Elliott, J.C. Structure and chemistry of the apatites and other calcium orthophosphates. *Stud. Org. Chem.* **1994**, *18*, 94008066.
4. Hughes, J.M.; Rakovan, J. The crystal structure of apatite, $Ca_5(PO_4)_3(F, OH, Cl)$. *Rev. Mineral. Geochem.* **2002**, *48*, 1–12. [[CrossRef](#)]
5. Gaft, M.; Reisfeld, R.; Panczer, G. *Modern Luminescence Spectroscopy of Minerals and Materials*; Springer: Berlin/Heidelberg, Germany, 2005.
6. Chindudsadeegul, P.; Jamkratoke, M. Effect of heat treatment on the luminescence properties of natural apatite. *Spectrochim. Acta Part A Mol. Biomol. Spectrosc.* **2018**, *204*, 276–280. [[CrossRef](#)] [[PubMed](#)]
7. Misiorowski, E.B. Jewelry of the 1990s. *Gems Gemol.* **2000**, *36*, 398–417. [[CrossRef](#)]
8. Chaipaksa, M. Apatite from Mozambique. *J. Gemmol.* **2015**, *34*, 654–655.
9. Zwaan, J.C. Apatite from Kenya. *J. Gemmol.* **2014**, *34*, 289–290.
10. Andrews, G.M. A few gem oddities. *J. Gemmol.* **1965**, *9*, 354–355.
11. Hyršl, J.; Petrov, A. Gemstones and ornamental stones from Bolivia: A review. *J. Gemmol.* **2002**, *26*, 41–47. [[CrossRef](#)]

12. Boyd, W.; Wight, W. Gemstones of Canada. *J. Gemmol.* **1983**, *18*, 544–556. [[CrossRef](#)]
13. Rahimzadeh, B.; Qeshlaqi, R.S. Apatite from Hormuz Island, Iran. *J. Gemmol.* **2016**, *35*, 6–7.
14. Johnston, C.; Bradshaw, J. Purple Apatite from Namibia. *J. Gemmol.* **2016**, *35*, 7–8.
15. Zwaan, J.C. Apatite from Durango, Mexico. *J. Gemmol.* **2019**, *36*, 683–684. [[CrossRef](#)]
16. Lakowan, J.; Laurs, B. Large Cat's-eye Apatite from Madagascar. *J. Gemmol.* **2016**, *35*, 186–188.
17. Laurs, B. Colourless Cat's-eye Apatite from Brazil. *J. Gemmol.* **2014**, *34*, 8.
18. Johnson, C. Cat's-eye Apatite from Namibia. *J. Gemmol.* **2014**, *34*, 191.
19. Kammerling, R.C.; Koivula, J.I.; Johnson, M.L.; Fritsch, E. Cat's-eye apatites from Madagascar. *Gems Gemol.* **1995**, *31*, 205–206.
20. Hyršl, J. Color-change apatite from Kazakhstan. *Gems Gemol.* **2002**, *38*, 350–351.
21. Young, E.J.; Myers, A.T.; Munson, E.L.; Conklin, N.M. Mineralogy and geochemistry of fluoapatite from Cerro de Mercado, Durango, Mexico. USGS Professional Paper. *Geol. Surv. Res.* **1969**, *650-D*, 84–93.
22. Krist, E.; Korikovsky, S.P.; Putiš, M.; Janák, M.; Faryad, S.W. *Geology and Petrology of Metamorphic Rocks of the Western Carpathian Crystalline Complexes*; Comenius University Press: Bratislava, Slovakia, 1992.
23. Putiš, M. Variscan and Alpidic nappe structures of the western Carpathian crystalline basement. *Geol. Carpathica* **1992**, *43*, 369–380.
24. Plašienka, D.; Grecula, P.; Putiš, M.; Kováč, M.; Hovorka, D. Evolution and structure of the Western Carpathians: An overview. In *Geological Evolution of the Western Carpathians (Mineralia Slovaca Monograph)*; Mineralia Slovaca: Košice, Slovakia, 1997.
25. Von Raumer, J.F.; Stampfli, G.M.; Bussy, F. Gondwana-derived microcontinents—The constituents of the Variscan and Alpine collisional orogens. *Tectonophysics* **2003**, *365*, 7–22. [[CrossRef](#)]
26. Bezák, V. Proposal of the new division of the West Carpathian crystalline based on the Hercynian tectonic building reconstruction. *Miner. Slovaca* **1994**, *26*, 1–6.
27. Putiš, M.; Filová, I.; Korikovsky, S.P.; Kotov, A.B.; Madarás, J. Layered metaigneous complex of the Veporic basement with features of the Variscan and Alpine thrust tectonics (the Western Carpathians). In *Geological Evolution of the Western Carpathians*; Grecula, P., Hovorka, D., Putiš, M., Eds.; Mineralia Slovaca Monograph: Bratislava, Slovakia, 1997; pp. 175–196.
28. Putiš, M.; Michálek, M.; Koller, F. Microtextures, P-T estimation and dating of metamorphic rocks exhumed in a Variscan shear zone, Veporic unit, Slovakia. In *Proceedings of the Petros Conference Proceedings*; Comenius University Press: Bratislava, Slovakia, 2011; pp. 28–32.
29. Hovorka, D.; Ivan, P.; Jaroš, J.; Kratochvíl, M.; Reichwalder, P.; Rojkovič, I.; Spišiak, J.; Turanová, L. *Ultramafic Rocks of the Western Carpathians*; GÚDŠ: Bratislava, Slovakia, 1985.
30. Putiš, M.; Sergeev, S.; Ondrejka, M.; Larionov, A.; Siman, P.; Spišiak, J.; Uher, P.; Paderin, I. Cambrian-Ordovician metaigneous rocks associated with Cadomian fragments in the West-Carpathian basement dated by SHRIMP on zircons: A record from the Gondwana active margin setting. *Geol. Carpathica* **2008**, *59*, 3.
31. Putiš, M.; Ivan, P.; Kohút, M.; Spišiak, J.; Siman, P.; Radvanec, M.; Uher, P.; Sergeev, S.; Larionov, A.; Méres, Š.; et al. Meta-igneous rocks of the West-Carpathian basement, Slovakia: Indicators of Early Paleozoic extension and shortening events. *Bulletin de la Société Géologique de France* **2009**, *180*, 461–471. [[CrossRef](#)]
32. Michálek, M.; Putiš, M. P-T-d evolution of eclogitic metabasites and Neoproterozoic orthogneiss in the North-Veporic basement of the central Western Carpathians. *Miner. Slovaca* **2009**, *41*, 1–22.
33. Putiš, M.; Frank, W.; Plašienka, D.; Siman, P.; Sulák, M.; Biroň, A. Progradation of the alpidic central Western Carpathians orogenic wedge related to two subductions: Constrained by $^{40}\text{Ar}/^{39}\text{Ar}$ ages of white micas. *Geodin. Acta* **2009**, *22*, 31–56. [[CrossRef](#)]
34. Klubert, J. *Muránska Dlhá Lúka, talc. Final Report*; ZSRP: Banská Štiavnica, Slovakia, 1955.
35. Geological Map of Slovakia M 1:50,000. Available online: <http://apl.geology.sk/gm50js> (accessed on 17 July 2020).
36. Bancík, T.; Krupa, M.; Sakmar, J.; Sečkář, P. Ojedinelý nález hydroxylapatitu na lokalite Muránska Dlhá Lúka. *Minerál* **2014**, *22*, 521–525.
37. Barrat, J.A.; Zanda, B.; Moynier, F.; Bollinger, C.; Liorzou, C.; Bayon, G. Geochemistry of CI chondrites: Major and trace elements, and Cu and Zn Isotopes. *Geochim. Cosmochim. Acta* **2012**, *83*, 79–92. [[CrossRef](#)]
38. Aufort, J.; Ségalen, L.; Gervais, C.; Brouder, C.; Balan, E. Modeling the attenuated total reflectance infrared (ATR-FTIR) spectrum of apatite. *Phys. Chem. Miner.* **2016**, *43*, 615–626. [[CrossRef](#)]

39. Antonakos, A.; Liarakapis, E.; Leventouri, T. Micro-Raman and FTIR studies of synthetic and natural apatites. *Biomaterials* **2007**, *28*, 3043–3054. [[CrossRef](#)] [[PubMed](#)]
40. Adams, D.M.; Gardner, I.R. Single-crystal vibrational spectra of apatite, vanadinite, and mimetite. *J. Chem. Soc. Dalton Trans.* **1974**, 1505–1509. [[CrossRef](#)]
41. Reisfeld, R.; Gaft, M.; Boulon, G.; Panczer, C.; Jørgensen, C.K. Laser-induced luminescence of rare-earth elements in natural fluor-apatites. *J. Lumin.* **1996**, *69*, 343–353. [[CrossRef](#)]
42. Bodył, S.; Czaja, M.; Mazurak, Z. Optical properties of Pr³⁺, Sm³⁺ and Er³⁺ ions in apatite, fluorite and phosphate glasses. *Phys. Procedia* **2009**, *2*, 515–525. [[CrossRef](#)]
43. Carnall, W.T.; Goodman, G.L.; Rajnak, K.; Rana, R.S. A systematic analysis of the spectra of the lanthanides doped into single crystal LaF₃. *J. Chem. Phys.* **1989**, *90*, 3443–3457. [[CrossRef](#)]
44. Mayer, I.; Diab, H.; Reinen, D.; Albrecht, C. Manganese in apatites, chemical, ligand-field and electron paramagnetic resonance spectroscopy studies. *J. Mater. Sci.* **1993**, *28*, 2428–2432. [[CrossRef](#)]
45. Gilinskaya, L.G.; Mashkovtsev, R.I. Blue and green centers in natural apatites by ERS and optical spectroscopy data. *J. Struct. Chem.* **1995**, *36*, 76–86. [[CrossRef](#)]
46. Fleet, M.E.; Pan, Y. Site preference of rare earth elements in fluorapatite: Binary (LREE+HREE)-substituted crystals. *Am. Mineral.* **1997**, *82*, 870–877. [[CrossRef](#)]
47. Hughes, J.M.; Cameron, M.; Mariano, A.N. Rare-earth-element ordering and structural variations in natural rare-earth-bearing apatites. *Am. Mineral.* **1991**, *76*, 1165–1173.
48. Fleet, M.E.; Pan, Y. Crystal chemistry of Rare Earth Elements in fluorapatite and some calc-silicates. *Eur. J. Mineral.* **1995**, *7*, 591–606. [[CrossRef](#)]
49. Fleet, M.E.; Pan, Y. Site preference of rare earth elements in fluorapatite. *Am. Mineral.* **1995**, *80*, 329–335. [[CrossRef](#)]
50. Ito, J. Silicate Apatites and Oxyapatites. *Am. Mineral.* **1968**, *53*, 890–907.
51. Felsche, J. Rare earth silicates with the apatite structure. *J. Solid State Chem.* **1972**, *5*, 266–275. [[CrossRef](#)]
52. Roeder, P.L.; Macarthur, D.; Ma, X.D.; Palmer, G.R.; Mariano, A.N. Cathodoluminescence and microprobe study of rare-earth elements in apatite. *Am. Mineral.* **1987**, *72*, 801–811.
53. Ronsbo, J.G. Coupled substitutions involving REEs and Na and Si in apatites in alkaline rocks from the Ilimaussaq intrusion, South Greenland, and the petrological implications. *Am. Mineral.* **1989**, *74*, 896–901.
54. Comodi, P.; Liu, Y.; Stoppa, F.; Woolley, A.R. A multi-method analysis of Si-, S- and REE -rich apatite from a new find of kalsilite-bearing leucitite (Abruzzi, Italy). *Mineral. Mag.* **1999**, *63*, 661–672. [[CrossRef](#)]
55. Cherniak, D.J. Rare earth element diffusion in apatite. *Geochim. Cosmochim. Acta* **2000**, *64*, 3871–3885. [[CrossRef](#)]
56. Chen, N.; Pan, Y.; Weil, J.A.; Nilges, M.J. Electron paramagnetic resonance spectroscopic study of synthetic fluorapatite: Part II. Gd³⁺ at the Ca1 site, with a neighboring Ca2 vacancy. *Am. Mineral.* **2002**, *87*, 47–55. [[CrossRef](#)]
57. Chen, N.; Pan, Y.; Weil, J.A. Electron paramagnetic resonance spectroscopic study of synthetic fluorapatite: Part I. Local structural environment and substitution mechanism of Gd³⁺ at the Ca2 site. *Am. Mineral.* **2002**, *87*, 37–46. [[CrossRef](#)]
58. Pan, Y.; Fleet, M.E. Compositions of the apatite-group minerals: Substitution mechanisms and controlling factors. *Rev. Mineral. Geochem.* **2002**, *48*, 13–49. [[CrossRef](#)]
59. Schroeder, L.W.; Mathew, M. Cation ordering in Ca₂La₈(SiO₄)₆O₂. *J. Solid State Chem.* **1978**, *26*, 383–387. [[CrossRef](#)]
60. Piriou, B.; Fahmi, D.; Dexpert-Ghys, J.; Taitai, A.; Lacout, J.L. Unusual fluorescent properties of Eu³⁺ in oxyapatites. *J. Lumin.* **1987**, *39*, 97–103. [[CrossRef](#)]
61. Suitch, P.R.; LaCout, J.L.; Hewat, A.; Young, R.A. The structural location and role of Mn²⁺ partially substituted for Ca²⁺ in fluorapatite. *Acta Crystallogr. Sect. B* **1985**, *41*, 173–179. [[CrossRef](#)]
62. Taitai, A.; Lacout, J.L. On the coupled introduction of Eu³⁺ and S²⁻ ions into strontium apatites. *J. Phys. Chem. Solids* **1989**, *50*, 851–855. [[CrossRef](#)]
63. Baran, E.J.; Baud, G.; Besse, J.-P. Vibrational spectra of some rhenium-apatites containing ReO₅-groups. *Spectrochim. Acta Part A Mol. Spectrosc.* **1983**, *39*, 383–386. [[CrossRef](#)]
64. Hitmi, N.; LaCabanne, C.; Bonel, G.; Roux, P.; Young, R.A. Dipole co-operative motions in an A-type carbonated apatite, Sr₁₀(AsO₄)₆CO₃. *J. Phys. Chem. Solids* **1986**, *47*, 507–515. [[CrossRef](#)]
65. Gruner, J.W.; McConnell, D. The problem of the carbonate-apatites. *Z. Krist.* **1937**, *97A*, 208–215.
66. Suetsugu, Y.; Takahashi, Y.; Okamura, F.P.; Tanaka, J. Structure analysis of A-type carbonate apatite by a single-crystal X-ray diffraction method. *J. Solid State Chem.* **2000**, *155*, 292–297. [[CrossRef](#)]

67. Ondrejka, M.; Bačík, P.; Putiš, M.; Uher, P.; Mikuš, T.; Luptáková, J.; Ferenc, Š.; Smirnov, A. Carbonate-bearing phosphohedyphane–“hydroxylphosphohedyphane” and cerussite: Supergene products of galena alteration in permian aplite (Western Carpathians, Slovakia). *Can. Mineral.* **2020**, *58*, 347–365. [[CrossRef](#)]
68. El Feki, H.; Savariault, J.M.; Salah, A. Ben Structure refinements by the Rietveld method of partially substituted hydroxyapatite: $\text{Ca}_9\text{Na}_{0.5}(\text{PO}_4)_{4.5}(\text{CO}_3)_{1.5}(\text{OH})_2$. *J. Alloys Compd.* **1999**, *287*, 114–120. [[CrossRef](#)]
69. Ivanova, T.I.; Frank-Kamenetskaya, O.V.; Kol'tsov, A.B.; Ugol'kov, V.L. Crystal structure of calcium-deficient carbonated hydroxyapatite. Thermal decomposition. *J. Solid State Chem.* **2001**, *160*, 340–349. [[CrossRef](#)]
70. Fleet, M.E.; Liu, X. Accommodation of the carbonate ion in fluorapatite synthesized at high pressure. *Am. Mineral.* **2008**, *93*, 1460–1469. [[CrossRef](#)]
71. Fleet, M.E.; Liu, X. Coupled substitution of type A and B carbonate in sodium-bearing apatite. *Biomaterials* **2007**, *28*, 916–926. [[CrossRef](#)]
72. Nash, W.P. Phosphate minerals in terrestrial igneous and metamorphic rocks. In *Phosphate Miner*; Springer: Berlin/Heidelberg, Germany, 1984; pp. 215–241.
73. Budzinski, H.; Tischendorf, G. Distribution of REE among minerals in the Hercynian postkinematic granites of Westerzgebirge-Vogtland, GDR. *Z. Geol. Wiss.* **1989**, *17*, 1019–1031.
74. O'Reilly, S.Y.; Griffin, W.L. Mantle metasomatism beneath western Victoria, Australia: I. Metasomatic processes in Cr-diopside lherzolites. *Geochim. Cosmochim. Acta* **1988**, *52*, 433–447. [[CrossRef](#)]
75. Kempe, U.; Götze, J. Cathodoluminescence (CL) behaviour and crystal chemistry of apatite from rare-metal deposits. *Mineral. Mag.* **2002**, *66*, 151–172. [[CrossRef](#)]
76. Waychunas, G.A. Apatite luminescence. *Rev. Mineral. Geochem.* **2019**, *48*, 701–742. [[CrossRef](#)]
77. Gaab, A.S.; Janák, M.; Poller, U.; Todt, W. Alpine reworking of Ordovician protoliths in the Western Carpathians: Geochronological and geochemical data on the Muráň Gneiss Complex, Slovakia. *Lithos* **2006**, *87*, 261–275. [[CrossRef](#)]
78. Uher, P.; Janák, M.; Ozdín, D. Calcian dravite from metacarbonate rocks of the Mútnik magnesite-talc deposit, Hnúšť'a, Slovakia. *Neues Jahrbuch für Mineralogie-Monatshefte* **2002**, *2002*, 68–84. [[CrossRef](#)]
79. Chew, D.M.; Babechuk, M.G.; Cogné, N.; Mark, C.; O'Sullivan, G.J.; Henrichs, I.A.; Doepke, D.; McKenna, C.A. (LA,Q)-ICPMS trace-element analyses of Durango and McClure Mountain apatite and implications for making natural LA-ICPMS mineral standards. *Chem. Geol.* **2016**, *435*, 35–48. [[CrossRef](#)]
80. Rossman, G.R. Apatite Spectra. Available online: <http://minerals.gps.caltech.edu/FILES/Visible/Apatite/Index.html> (accessed on 5 October 2020).

Publisher's Note: MDPI stays neutral with regard to jurisdictional claims in published maps and institutional affiliations.



© 2020 by the authors. Licensee MDPI, Basel, Switzerland. This article is an open access article distributed under the terms and conditions of the Creative Commons Attribution (CC BY) license (<http://creativecommons.org/licenses/by/4.0/>).